Optics Letters

Compact snapshot optically replicating and remapping imaging spectrometer (ORRIS) using a focal plane continuous variable filter

Tingkui Mu,[1,2,*] Feng Han,[1,2] Donghao Bao,[1,2] Chunmin Zhang,[1,2] and Rongguang Liang[3]

[1]Institute of Space Optics, School of Science, Xi'an Jiaotong University, Xi'an, Shaanxi 710049, China
[2]Key Laboratory for Nonequilibrium Synthesis and Modulation of Condensed Matter (Xi'an Jiaotong University), Ministry of Education, Xi'an, Shaanxi 710049, China
[3]College of Optical Sciences, University of Arizona, Tucson, Arizona 85721, USA
*Corresponding author: tkmu@mail.xjtu.edu.cn

Received 3 January 2019; revised 5 February 2019; accepted 5 February 2019; posted 6 February 2019 (Doc. ID 356576); published 1 March 2019

In this Letter, a novel snapshot spectral imaging technique, optically replicating and remapping imaging spectrometer, is presented. It is based on the combination of shifting subimages by a specially designed lenslet array (LA) and filtering subimages by a focal plane continuous variable filter (CVF). The 3D datacube is recovered by just using a simple image remapping process. The use of the LA and the focal plane CVF makes the system compact and low in cost. A handheld proof-of-principle prototype has been built and demonstrated; it covers a wavelength range of 380–860 nm with 80 spectral channels with a spatial resolution of 400 × 400 pixels.

https://doi.org/10.1364/OL.44.001281

Snapshot spectral imaging is powerful for the acquisition of a three-dimensional (3D) datacube (x, y, λ), including two-dimensional spatial (x, y) and one-dimensional spectral (λ), within a single integration time [1–4]. It has the capability of capturing dynamic objects or the static objects located at dynamic environments without any scanning mechanism. So far, diverse snapshot spectral imaging techniques have been developed, such as the computed tomography imaging spectrometer (CTIS) [5], coded aperture snapshot spectral imaging (CASSI) [6], the multispectral Sagnac interferometer (MSI) [7], snapshot hyperspectral imaging Fourier transform (SHIFT) [8], integration-field spectroscopy (IFS) [9–16], the image mapping spectrometer (IMS) [17], and the image-replicating imaging spectrometer (IRIS) [18]. While the CTIS, CASSI, MSI, and SHIFT rely on iterative reconstruction algorithms for recovering a 3D datacube, IFS, IMS, and IRIS directly obtain spectral images. Most of these techniques employ dispersive or interferometric elements to separate spectra, leading to a bulky system.

Filtering the spectra with bandpass filters is one of the simplest and low-cost methods for spectral imaging [19]. Color filter arrays [20] and multispectral filter arrays [21,22] are two typical examples [23–26]. While the system can be compact, the measurable spectral bands are limited by the number of the filters in the system. The continuous variable filter (CVF) [27–29] is a relatively new type of spectral filter and has been used for hyperspectral imaging. It can be mounted on the surface of a focal plane array (FPA) [30], or be directly deposited on an FPA as a robust integration [31–33]. Most spectral imaging systems with the focal plane CVFs use a single imaging lens, and the scanning mechanism is needed to form a 3D datacube. [27–34]. Recently, the CVF was inserted into the aperture plane to achieve snapshot spectral imaging using a light field imaging concept [35]. However, the CVF's continuous spectral feature was not fully utilized; only 27 spectral channels were achieved. Further, the spatial sampling density is limited, since the Nyquist sampling theorem is determined by the micro-lens pitch instead of pixel pitch.

In patent applications [36,37] we presented the concept of a snapshot optically replicating and remapping imaging spectrometer (ORRIS) using the focal plane CVF. By replacing the single imaging lens in the scanning system with a specially designed lenslet array (LA), the 3D datacube can be acquired within a single snapshot and recovered with a simple image remapping process. Herein, the principle and the prototype of the ORRIS system are presented.

The compact ORRIS system is depicted in Fig. 1(a). It composes an LA of $(M + 1) \times N$ lenslets with lateral-shift columns and a common rectangular CVF on the surface of FPA. To avoid the crosstalk between the lenslets, a baffle array should be placed between the LA and CVF. As shown in Fig. 1(b), the lenslet arrays are not distributed in a square or rectangular grid, but in a staircase grid. It is specially designed to shift the replicated subimages perpendicular to the constant spectral transmission line (or waveband) of the CVF to obtain spectral information at each pixel. The shift distance of each column lenslets or the tilt angle θ between the row direction of LA and the waveband direction of the CVF determines the spectral resolution of the system. The replicated column subimages are laterally shifted and continuously filtered by the spectral gradient of the CVF, as depicted in Fig. 1(c). Different spatial rows

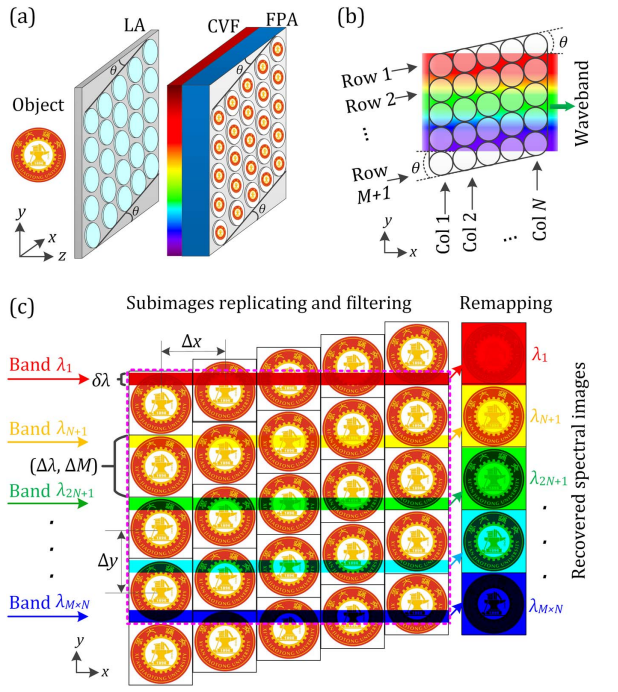

Fig. 1. (a) Schematic of the ORRIS system. (b) LA is a staircase grid, and there is an angle θ between the row direction and waveband direction. (c) Replicating and filtering processing of subimages, and the remapping of spectral images at each band. The dotted pink rectangle indicates the area of the FPA.

of each subimage correspond to different central wavelengths. The same central wavelength λ_i with a bandwidth of $\delta\lambda$ covers the adjacent spatial content in each subimage in the same row. Then spatio-spectral subimages are acquired in a single exposure time on the FPA. The spectral image at each λ_i is finally recovered using the simple image remapping process. No complex iterative reconstruction algorithm is required.

Assuming that the bandwidth and pixel number covered by a subimage are $\Delta\lambda$ and ΔM along the spectral gradient y, theoretically, the resolvable bandwidth will be $\delta\lambda = \Delta\lambda/\Delta M$. However, if we increase ΔM to increase the spatial resolution, the number of detectable subimages will be reduced due to the limited size of an FPA. As a result, a row of staircase grids may not fully scan the bandwidth $\delta\lambda$. To maximize the spatial resolution of each subimage and completely sample the $\delta\lambda$ by a row of subimages, the relationship $N \le \Delta M$ should be met, where N is the column number of LA. Correspondingly, the minimum resolvable bandwidth becomes $\delta\lambda = \Delta\lambda/N$, and the angle θ between the row direction of LA and the waveband direction of CVF is $\theta = \tan^{-1}[\Delta y/(N \times \Delta x)]$, where Δx and Δy indicate the pitches of subimages along the x and y directions, respectively. The field of view (FOV) can be rectangular with $\Delta x \neq \Delta y$ [24]. For the square FOV, $\Delta x = \Delta y$, and $\theta = \tan^{-1}(1/N)$. If the row number of the LA covered by an FPA is M, the detectable spectral range of the system would be $\Delta\lambda' = M \times N \times \delta\lambda$. That means the number of available spectral channels is $C = M \times N$ with the bandwidth of $\delta\lambda$. To fully utilize the effective size of the FPA indicated by the dotted pink rectangle in Fig. 1(c), there must be some dead zones covered by the top and bottom rows of the lenslets. The sum of the invalid zones is equivalent to the area covered by a row of lenslets. The dimension of the obtained 3D datacube depends on the sizes of the FPA and CVF, and the number of lenslets. There is a tradeoff between the spatial and spectral resolution, the spectral resolution increases with the number of lenslets, and the spatial resolution is the opposite.

To the best of our knowledge, the technique of utilizing a CVF in conjunction with an LA was reported recently [38]. However, the principle and performance are different. The reported method places the CVF at the aperture plane, and the CVF works as a bandpass filter with a different transmission band in front of each lenslet; therefore, the advantage of gradient spectral transmission is totally lost. In contrast, our proposed method places the CVF in front of the FPA; the spectral bandwidth received by each pixel is narrower, depending on the $F\#$ of the lenslet and the distance between the CVF and FPA.

Note that the thin system in Fig. 1(a) adapts only to infinite imaging. For finite imaging, there will be a parallax issue for each lenslet. As a result, the common spatial content on each subimage will be reduced, and the continuous spectral filtering will be destroyed. The ORRIS system for general imaging is presented in Fig. 2(a). A fore relay optical system, including an objective lens (OL) and a collimating lens (CL), is attached. A field stop (FS) located at the intermediate image plane is to limit the FOV and, thus, avoid the crosstalk between the subimages. In this case, the baffle array is not needed between the LA and CVF. The proof-of-principle prototype was built in Fig. 2(b). The combination of the OL (Navitar EF 50 mm, $f/0.95$) and the CL (Navitar EF 50 mm, $f/0.95$) is used for collimating the incident light originated from the target. The area of the intermediate image is limited by the FS. The LA reimages the intermediate image onto the CVF and the FPA. The CVF is a commercial off-the-shelf element with an effective size of 25×30 mm (Delta, LVVISNIRBP25), as shown in the upper right inset of Fig. 2(b). Its nominal central wavelength ranges from 450 to 850 nm along the 25 mm side with nominal full width at half-maximum (FWHM) of 4% central wavelengths. The FPA is a 3232×4864 CCD array (AVT, Prosilica GT 4907) with $7.4\ \mu\text{m} \times 7.4\ \mu\text{m}$ pixels. The sensor size of 24×36 mm can maximally cover the effective size of the CVF. The LA is a 9×10 array composed of 90 off-the-shelf plano-convex lenslets that are made from N-BK7 glass (Edmund Optics, #23061), as shown in the upper middle inset of Fig. 2(b). They are mounted in a custom aluminum plate with an array of staircase holes, and each column has a lateral shift of 0.3 mm. The lenslet has a focal length of 12 mm and a diameter of 3 mm. The lenslet pitches are 3 mm along the x and y directions for adapting to the square FS. Accordingly, the tilt angle is $\theta \approx 5.71°$. The spatial resolution

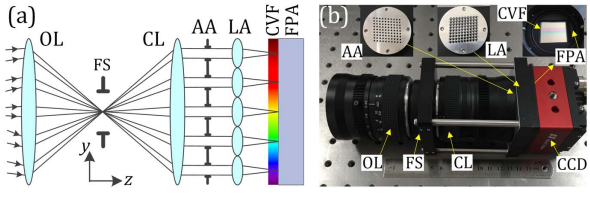

Fig. 2. (a) Optical schematic of the ORRIS system for general imaging application, and (b) the proof-of-principle prototype. OL, objective lens; FS, field stop; CL, collimating lens; AA, aperture array; LA, lens array; CVF, continuous variable filter; and FPA, focal plane array.

of each subimage is about 400 × 400. To improve the imaging quality over marginal fields, an aperture array (AA) with a diameter of 1.5 mm is placed in front of the LA, as shown in the upper left inset of Fig. 2(b), leading to a *F#* of 8 for each lenslet. The higher the *F#*, the narrower the FWHM and the smaller the shift of the central wavelength of the CVF, because the FWHM and central wavelength of the CVF depend on the incident angle [30]. However, optical efficiency will become lower with a smaller subaperture. Note that most elements in ORRIS are off-the-shelf products, except the mount for LA.

Image registration, spectral calibration, flatfield, and radiometric calibration should be implemented before constructing a spectral image. To register subimages, a target containing many feature points is imaged by ORRIS. One of the central subimages is selected as the reference image, and other subimages are adjusted to match the reference image. A sub-pixel spatial registration algorithm in *Matlab* is employed to determine the registration coefficients.

The aim of spectral calibration is to assign the pixels on the FPA to a unique wavelength. First, a broadband uniform area source is generated by illuminating an integrating sphere with a tungsten lamp and a mercury lamp simultaneously. Then the uniform area source at the exit port of the sphere is filtered by four 1 nm bandpass filters centered at 488, 514, 532, and 633 nm sequentially, and measured by an ORRIS and a reference Vis/NIR spectrometer (ASD, FieldSpec 3). After combining the images of four wavelengths measured by the ORRIS, the spectral curve of each spatial point across the FOV is extracted. By comparing these spectral curves to the ASD's data, we see that the peak positions of the four wavelengths on each curve are identified using a Gaussian fit every 1 nm, and the positions of other wavelengths are interpolated. Finally, all determined wavelength positions on the curve are projected to the pixel positions using a polynomial curve fitting, and the transformation coefficients with pixel indices are applied to all subsequent measurements.

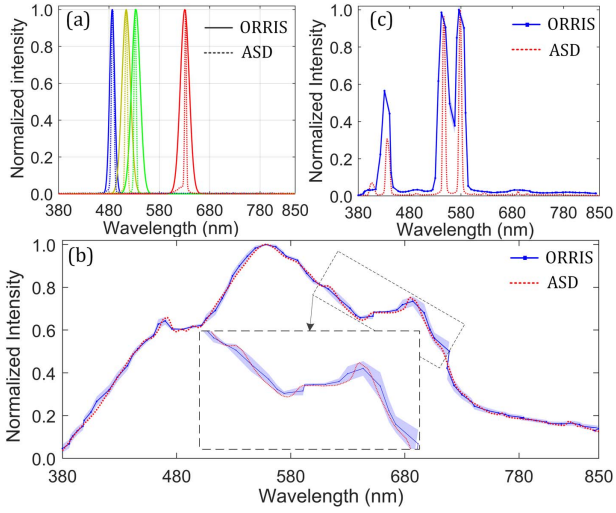

Fig. 3. Spectra of (a) four narrowband filters centered at 488, 514, 532, and 633 nm; (b) a broadband source, and (c) a high-pressure mercury lamp measured by the ORRIS (solid line) and an ASD spectrometer (dotted line), respectively. The blue shaded bounds indicate standard deviations across the FOV. The curves in the black dashed boxes in (b) are magnified for displaying deviations.

Figure 3(a) shows that the calibration results correspond to the average of all spatial points across the FOV of the ORRIS. It is found that the spectral region is extended to 380–850 nm from the CVF vendor's nominal region of 450–850 nm mainly due to the non-normal incidence of rays [30]. The peaks measured by the ASD and ORRIS are consistent with the filter's nominal values. The FWHMs measured by the ORRIS at each wavelength are 16.6 ± 0.8, 18.3 ± 0.5, 18.4 ± 0.6, and 21.7 ± 0.8 nm, respectively, approaching to the CVF vendor's nominal values of about 4% central wavelengths.

The flatfield image is captured from the broadband uniform area source. The spectral curve corresponding to the average of all spatial points across the FOV is considered as a reference. Subtracting the dark frame and dividing this reference curve by all spectral curves normalizes the intensity. The normalization coefficients are used to all subsequent measurements. For the radiometric calibration, the broadband source is also measured by the ASD. By fitting the spectral curve of each spatial point to the ASD's data, the derived calibration coefficients are then applied to all subsequent measurements. The flatfield and radiometric calibration also can be integrated into one common process. Figure 3(b) shows the measured broadband spectrum that corresponds to the average value of all spatial points across the FOV. The shaded bounds indicate the standard deviations of all spatial points relative to the average value, and they are less than 0.05. The relative errors between the average spectrum and the ASD's data are below 4.7% over the working range. The error is mainly caused by the imperfect lateral shift of lenslets due to the error in fabricating the aluminum mount for the lenslet array, especially at the edge region. This may be improved in the future with a custom LA. Figure 3(c) shows the measured spectrum when a high-pressure mercury lamp was used to illuminate the integrating sphere. While the three main peaks (436, 547, and 579 nm) are resolved, the small peak (406 nm) is discarded due to weak efficiency.

To demonstrate the spectral imaging capability, two types of scenes are imaged: static and dynamic. Figure 4 shows a portion of imaging results of a static scene that was captured in a cloudy

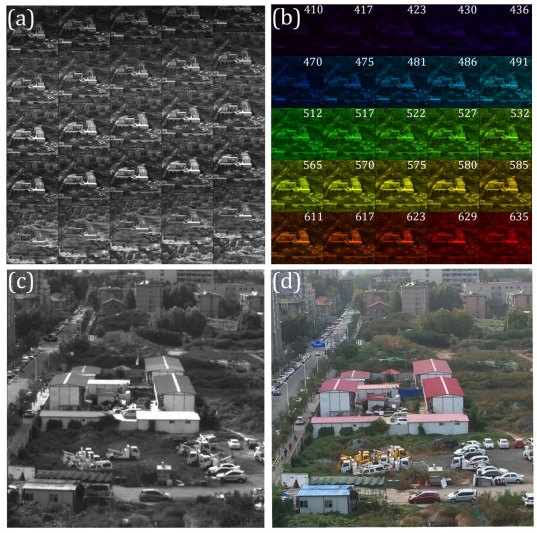

Fig. 4. Image results of a static scene. (a) Original shifted gray subimages, (b) remapped spectral images, (c) a single gray subimage, and (d) the RGB image of the similar scene captured by a cell phone.

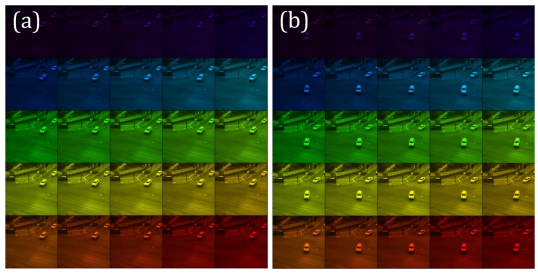

Fig. 5. Image results of a dynamic scene (Visualization 1, Visualization 2, and Visualization 3). (a) First and (b) the second snapshot spectral images extracted from the Visualization 1 which shows 80 remapped spectral videos. Visualization 2 shows the original 80 spatio-spectral gray subimages captured at video rate, and Visualization 3 shows one of the gray subimages.

day. Figure 4(a) shows 25 selected raw gray spatio-spectral subimages of the total 80 subimages. With the image remapping process, the reconstructed continuously spectral images are shown in Fig. 4(b); 25 spectral channels of the total 80 channels are displayed. Figure 4(c) is the single gray subimage. For comparison, the RGB image of the similar scene captured by a cell phone is presented in Fig. 4(d). Since the RGB image was captured at a different day, there is slight difference between the images. As can be seen, the scene includes complex objects, and the spatial resolution is good enough to recognize them. Figure 5 shows the remapped spectral images for a dynamic scene (see Visualization 1 for the total 80 remapped spectral videos, Visualization 2 for the original 80 spatio-spectral gray subimages captured at video rate, and Visualization 3 for one of the gray subimages). The moving automobiles at a crossroads were captured in real time.

In conclusion, we have presented a novel snapshot spectral imaging technique, ORRIS, using a focal plane CVF. A proof-of-principle prototype was built using off-the-shelf components. The ORRIS prototype can capture 80 continuous spectral channels over the spectral region of 380–850 nm with a spatial resolution 400 × 400 pixels in a single integration time. For general imaging applications, the volume of the prototype is about 230 mm (length) ×70 mm (width) ×70 mm (height), and the weight is about 1.0 kg. Most of the space and weight are due to the fore relay lenses. For infinite imaging applications, the fore lenses can be removed, and the system volume will become 50 mm (length) ×70 mm (width) ×70 mm (height) and 0.5 kg. The volume can be reduced further by using a small camera and relay optics, and the infrared spectral region can be extended to 950 nm [29].

Note that the system can be reconfigured with a dense LA to capture more spectral channels, such as 140 channels with a spatial resolution 300 × 300 pixels or 320 channels with 200 × 200 pixels. However, the FWHM at each channel is limited by CVF itself [29,30]. To reduce spectral mixing in some applications, the number of spectral channels should match to the FWHM of each channel. Further, since ORRIS uses the LA for the division of aperture, the optical efficiency of each subaperture becomes lower relative to the scanning system with a single large aperture [27–34].

The ORRIS system has potential applications in industrial inspection and machine vision which usually need the snapshot capability. It may also find diverse applications in micro-unmanned aerial vehicles or ground vehicles for surveillance. Furthermore, it can be used for biomedical diagnosis by conveniently adapting to the commercial microscopies, such as fluorescence microscopy and confocal microscopy, ophthalmoscopes, endoscopes, and laryngoscopes.

Funding. National Natural Science Foundation of China (NSFC) (61775176, 61405153, 41530422); Fundamental Research Funds for the Central Universities of China (xjj2017105).

REFERENCES

1. N. Hagen, R. T. Kester, L. Gao, and T. S. Tkaczyk, Opt. Eng. **51**, 111702 (2012).
2. N. Hagen and M. W. Kudenov, Opt. Eng. **52**, 090901 (2013).
3. L. Gao and R. T. Smith, J. Biophotonics **8**, 441 (2015).
4. L. Gao and L. V. Wang, Phys. Rep. **616**, 1 (2016).
5. M. Descour and E. Dereniak, Appl. Opt. **34**, 4817 (1995).
6. A. A. Wagadarikar, N. P. Pitsianis, X. Sun, and D. J. Brady, Opt. Express **17**, 6368 (2009).
7. M. W. Kudenov, M. E. L. Jungwirth, E. L. Dereniak, and G. R. Gerhart, Appl. Opt. **49**, 4067 (2009).
8. M. W. Kudenov and E. L. Dereniak, Opt. Express **20**, 17973 (2012).
9. J. Allington-Smith, New Astron. Rev. **50**, 244 (2006).
10. J. G. Dwight and T. S. Tkaczyk, Biomed. Opt. Express **8**, 1950 (2017).
11. Y. Wang, M. E. Pawlowski, and T. S. Tkaczyk, Opt. Eng. **56**, 081803 (2017).
12. J. Allington-Smith and R. Content, Publ. Astron. Soc. Pac. **110**, 1216 (1998).
13. R. Content, S. Blake, C. Dunlop, D. Nandi, R. Sharples, G. Talbot, T. Shanks, D. Donoghue, N. Galiatsatos, and P. Luke, Remote Sens. **5**, 1204 (2013).
14. A. Bodkin, A. Sheinis, A. Norton, J. Daly, S. Beaven, and J. Weinheimer, Proc. SPIE **7334**, 73340H (2009).
15. T. Mu, C. Zhang, Q. Li, Y. Wei, Q. Chen, and C. Jia, Proc. SPIE **9298**, 92980D (2014).
16. T. Mu, S. Pacheco, Z. Chen, C. Zhang, and R. Liang, Sci. Rep. **7**, 42115 (2017).
17. L. Gao, R. T. Kester, N. Hagen, and T. S. Tkaczyk, Opt. Express **18**, 14330 (2010).
18. A. Gorman, D. W. Fletcher-Holmes, and A. R. Harvey, Opt. Express **18**, 5602 (2010).
19. P. Lapray, X. Wang, J. Thomas, and P. Gouton, Sensors **14**, 21626 (2014).
20. L. Anzagira and E. R. Fossum, J. Opt. Soc. Am. A **32**, 28 (2015).
21. M. R. Kutteruf, M. K. Yetzbacher, M. J. DePrenger, K. M. Novak, C. A. Miller, T. V. Downes, and A. V. Kanaev, Appl. Opt. **53**, C45 (2014).
22. B. Geelen, N. Tack, and A. Lambrechts, Proc. SPIE **8974**, 89740L (2014).
23. B. Geelen, N. Tack, and A. Lambrechts, Proc. SPIE **8613**, 861314 (2013).
24. N. Gupta, P. R. Ashe, and S. Tan, Opt. Eng. **50**, 033203 (2011).
25. S. A. Mathews, Appl. Opt. **47**, F71 (2008).
26. Y. Oiknine, I. August, and A. Stern, Opt. Lett. **43**, 5042 (2018).
27. A. M. Mika, Proc. SPIE **1298**, 127 (1990).
28. G. T. Elerding, J. G. Thunen, and L. M. Woody, Proc. SPIE **1479**, 380 (1991).
29. O. Pust, Opt. Photonics **11**, 24 (2016).
30. I. G. E. Renhorn, D. Bergström, J. Hedborg, D. Letalick, and S. Möller, Opt. Eng. **55**, 114105 (2016).
31. N. Tack, A. Lambrechts, P. Soussan, and L. Haspeslagh, Proc. SPIE **8266**, 82660Q (2012).
32. T. Skauli, H. E. Torkildsen, S. Nicolas, T. Opsahl, T. Haavardsholm, I. Kåsen, and A. Rognmo, Appl. Opt. **53**, C64 (2014).
33. L. Wei, X. Xiao, W. Yueming, Z. Xiaoqiong, and L. Junwei, Proc. SPIE **9880**, 98802F (2016).
34. Y. Xu, J. Li, C. Bai, H. Yuan, and J. Liu, Opt. Lett. **43**, 4081 (2018).
35. R. Horstmeyer, R. Athale, and G. Euliss, Proc. SPIE **7468**, 746804 (2009).
36. T. Mu, "Compact miniature snapshot spectral imaging systems and methods," Chinese patent application CN107271039A (July13, 2017).
37. T. Mu, Z. Chen, and C. Zhang, "Compact miniature snapshot channeled polarimetric spectral imaging systems and methods," Chinese patent CN107228711 B (July13, 2017).
38. M. Hubold, R. Berlich, C. Gassner, R. Brüning, and R. Brunner, Proc. SPIE **10545**, 105450V (2018).